

# A membrane-free electrochemical reactor for efficient oxygen removal via gravity-assisted product self-separation

Received: 27 January 2025

Accepted: 24 April 2025

Published online: 08 May 2025

Check for updates

Peng Li<sup>1,2,7</sup>, Xin Tang<sup>3,7</sup>, Xin Zhou<sup>4,7</sup>, Changming Zhao<sup>5</sup>, Wanyu Shen<sup>1</sup>, Yi Tan<sup>1</sup>, Deming Li<sup>1</sup>, Peng Jiang<sup>1</sup>, Fangyao Zhou<sup>1</sup>, Zhe Wang<sup>4</sup>, Jun Tang<sup>1</sup>✉, Guiqiang Li<sup>3</sup>✉, Yu Zhang<sup>1,2,6</sup>✉ & Yuen Wu<sup>1,2,6</sup>✉

Although electrochemical technologies offer vast industrial prospects, broader adoption—particularly in consumer applications—remains constrained by high costs and limited component lifespans. Here, we present a gravity-assisted, membrane-free electrochemical oxygen (O<sub>2</sub>) removal (EOR) reactor coupling oxygen reduction (ORR) and oxygen evolution (OER) reactions. Leveraging fluid mechanics insights, buoyant O<sub>2</sub> bubbles ascend rapidly, achieving 95% product self-separation and eliminating the need for membranes or external circulation. To withstand high hydrostatic pressures and ensure a 10-year operational lifespan, we developed an integrative gas diffusion electrode (GDE) with ~85.5% conductivity and 80.2% gas permeability relative to conventional carbon paper, yet 2.2-fold higher mechanical strength and 30-fold greater stability. In a household refrigerator, our two-cell system boosts fresh-keeping capacity by 3.4-fold. Comprehensive economic analysis reveals a 22.6-fold increase in O<sub>2</sub> removal per unit cost compared with ion-exchange membrane-based reactors, underscoring this design's cost-effective, long-lived potential for diverse real-world applications.

Electrochemical technology presents significant potential across diverse fields, including gas purification, chemical synthesis, environmental remediation, and precision-controlled storage. Its primary advantages—such as high energy efficiency and scalability—have spurred extensive research and industrial investments in recent decades<sup>1–4</sup>. Despite these promising attributes, the widespread adoption of electrochemical reactors is hindered by two major challenges. First, many existing electrochemical reactor designs depend on high-cost ion-exchange membranes, which not only increase initial capital expenditure but also suffer from limited operational lifetimes, rendering them unsuitable for applications requiring long-term operation

under fluctuating conditions<sup>5–7</sup>. Second, the complex designs of traditional electrochemical reactors often necessitate auxiliary gas supplies, circulation systems, and frequent maintenance<sup>8,9</sup>, posing a particular challenge for small-scale or consumer-oriented applications where compactness, affordability, and low maintenance are essential.

A compelling illustration of these challenges can be found in low-oxygen (O<sub>2</sub>) food storage, which extends shelf life by slowing oxidation and microbial growth, thereby preserving both freshness and nutrient content<sup>10,11</sup>. While household refrigerators have traditionally relied on low temperatures to mitigate spoilage, reducing O<sub>2</sub> levels in the storage environment provides a significant advantage, particularly for

<sup>1</sup>The Dermatology Department of The First Affiliated Hospital of USTC, Division of Life Sciences and Medicine, University of Science and Technology of China, Hefei 230001 Anhui, China. <sup>2</sup>Deep Space Exploration Laboratory/School of Chemistry and Materials Science, University of Science and Technology of China, Hefei 230026 Anhui, China. <sup>3</sup>Department of Thermal Science and Energy Engineering, University of Science and Technology of China, Hefei, Anhui 230026, China. <sup>4</sup>Hefei Hualing Co., Ltd, Hefei 230088, China. <sup>5</sup>Anhui Entropy Carnot Energy Technology Co., Ltd, Hefei 230031, China. <sup>6</sup>Key Laboratory of Precision and Intelligent Chemistry, University of Science and Technology of China, Hefei 230026 Anhui, China. <sup>7</sup>These authors contributed equally: Peng Li, Xin Tang, Xin Zhou. ✉e-mail: [tangjun0212@ustc.edu.cn](mailto:tangjun0212@ustc.edu.cn); [ligq@ustc.edu.cn](mailto:ligq@ustc.edu.cn); [zy11260@ustc.edu.cn](mailto:zy11260@ustc.edu.cn); [yuenwu@ustc.edu.cn](mailto:yuenwu@ustc.edu.cn)

nutrient-sensitive items such as fresh produce and meats. However, conventional O<sub>2</sub> removal methods—such as nitrogen flushing or membrane-based gas separation—often involve bulky equipment and exhibit low O<sub>2</sub> removal efficiency<sup>12–14</sup>, both of which conflict with the compact design and high-performance requirements of consumer appliances like refrigerators. In contrast, electrochemical technology has emerged as a promising, energy-efficient alternative, selectively removing O<sub>2</sub> from the environment via cathodic oxygen reduction (ORR). However, many current electrochemical systems still rely on ion-exchange membranes to separate reaction products or incorporate complex circulation mechanisms, thus increasing both system costs and maintenance demands. Moreover, the pivotal component in these systems—traditional carbon paper-based gas diffusion electrodes (GDE)—often suffers from suboptimal mechanical strength and operational stability over long-term operation, thereby severely limiting the broader application potential of conventional electrochemical setups<sup>15–17</sup>.

In this study, we introduce a gravity-assisted product self-separation reactor (GAPS Reactor) that addresses the above critical challenges through innovative reactor and electrode designs<sup>18,19</sup>. Guided by fluid mechanics insights showing that O<sub>2</sub> bubbles ascend rapidly. We harness these natural density gradients to enable product self-separation. In this reactor, the inherent density gradients among the electrode, liquid electrolyte, and gas phase enable spontaneous, buoyancy-driven O<sub>2</sub> migration from denser to less dense zones—effectively forming a self-organizing “O<sub>2</sub> ladder” that obviates the need for external pumping or membranes and realizes the self-separation of product. Second, to withstand high liquid pressure at the cathode in this reactor design, we have developed an integrative GDE whose electrical conductivity and gas permeability reach approximately 85.5 and 80.2%, respectively, of those of conventional carbon paper GDE, while its mechanical strength and operational stability exceed those of carbon paper by factors of 2.2 and 30, respectively. Accelerated aging tests indicate a potential service life of our GAPS Reactor of up to 10 years. A two-cell series-connected reactor was incorporated into a household refrigerator, resulting in a 3.4-fold improvement in its fresh-keeping capabilities. Economic analysis shows the reactor’s O<sub>2</sub> removal capacity per unit device cost is 22.6 times that of traditional ion-exchange membrane-based systems. Although validated in a refrigerator drawer, our GAPS system—bypassing the cost and maintenance of traditional designs—supports applications from food packaging to biomedicine, offering a practical blueprint for everyday electrochemical O<sub>2</sub> removal.

## Results

A key feature of our GAPS Reactor is its ability to spontaneously separate the reaction product (the O<sub>2</sub> gas)—by exploiting the density differences among the electrode (high density), the liquid electrolyte (medium density), and the gas phase (low density). To quantify this self-separation process from a fluid mechanics standpoint, we focus on the motion of O<sub>2</sub> bubbles generated at the anode (through the oxygen evolution reaction, OER) and how they ascend and exit the liquid surface under buoyancy.

When a small gas bubble (radius  $r$ ) forms and detaches from the anode surface, it experiences two primary forces in the electrolyte: the buoyant force ( $F_b$ ) and the viscous drag force ( $F_d$ ). The Reynolds number is given by:

$$Re = \frac{\rho_l v_b (2r)}{\mu_l} \quad (1)$$

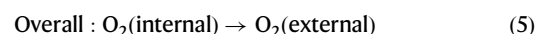
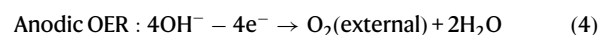
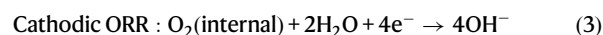
where  $\rho_l$  is the liquid density,  $v_b$  is the bubble’s rising speed,  $2r$  is the bubble’s diameter (taken as the characteristic length), and  $\mu_l$  is the liquid viscosity. Since the bubbles are generally small (on the order of millimeters or microns) and travel only a short distance before

reaching the surface, this approach provides a useful approximate baseline for predicting their motion. Accordingly, we employ the simplified Stokes formula (the derivation process is provided in the Methods section). If the bubble radius or fluid disturbances differ significantly from the assumed values, a more general resistance model or multiphase fluid dynamics simulation (CFD) would be required to obtain more accurate results.

$$v_b = \frac{2r^2(\rho_l - \rho_g)g}{9\mu_l} \quad (2)$$

Using a 20% potassium carbonate solution as the electrolyte ( $\rho_l \approx 1162 \text{ kg}\cdot\text{m}^{-3}$ ,  $\rho_g \approx 1.42 \text{ kg}\cdot\text{m}^{-3}$ ,  $\mu_l = 0.0013 \text{ Pa}\cdot\text{s}$ ) and  $r = 0.3\text{--}0.5 \text{ mm}$ ,  $g = 9.81 \text{ m}\cdot\text{s}^{-2}$ , the resulting velocity is  $\sim 0.175\text{--}0.486 \text{ m}\cdot\text{s}^{-1}$ . This implies that, for an anode depth of  $h = 0.05 \text{ m}$ , the time required for a bubble to reach the fluid surface is on the order of 0.10–0.28 s. The rapid upward transport of O<sub>2</sub> bubbles indicates that, once gas is generated at the anode, it quickly exits the reactor without the need for additional pumps or forced circulation. The density gradient across the high-density electrode region, the medium-density electrolyte, and the low-density gas headspace forms a “ladder” for O<sub>2</sub> migration. As a result, backflow or re-dissolution of O<sub>2</sub> is greatly suppressed, ensuring both high efficiency and long-term stability in the GAPS system.

Building on the fluid mechanics principle of buoyancy-driven bubble rise, we designed a GAPS Reactor for seamless integration into household refrigerators (Fig. 1). The reactor configuration consists of a porous nickel mesh anode located above the cathode, ensuring that O<sub>2</sub> generated at the anode forms bubbles that immediately enter the bulk electrolyte. The cathode, responsible for ORR, is positioned at the reactor’s base, a large-area open cathode design was implemented to overcome the mass transfer limitations resulting from the absence of a gas–liquid circulation system. Furthermore, the cathode interfaces directly with the low-O<sub>2</sub> storage environment through a mesh partition. The electrochemical reactions at the anode and cathode are as follows<sup>20–22</sup>:



The internal O<sub>2</sub> is reduced to OH<sup>−</sup>, which remains dissolved in the electrolyte. Because the buoyancy mechanism spontaneously separates O<sub>2</sub> from the liquid phase, no ion-exchange membrane or forced circulation is required, with the electrolyte serving as both the ion conduction medium and the gravitational separation medium. The cathode, being at the bottom of the module, must withstand substantial hydrostatic pressure, so we implemented an integrative GDE with enhanced mechanical strength and a stable pore structure, which will be discussed in the following content. This design establishes a self-organizing “O<sub>2</sub> ladder,” allowing bubbles to naturally ascend. By eliminating the need for costly membrane components or external pumping, we significantly reduce system complexity and operational costs while maintaining high O<sub>2</sub> removal efficiency. Furthermore, the minimized contact between O<sub>2</sub> bubbles and the low-O<sub>2</sub> zone at the cathode reduces unwanted reoxidation or backflow, enhancing the longevity and performance consistency of the reactor. In summary, our reactor utilizes bubble buoyancy to enable efficient, membrane-free O<sub>2</sub> removal.

Given the cathode’s pivotal role in withstanding elevated hydrostatic pressure, efficiently catalyzing ORR under low-O<sub>2</sub> conditions, and ensuring a 10-year operational lifespan, our next objective was to

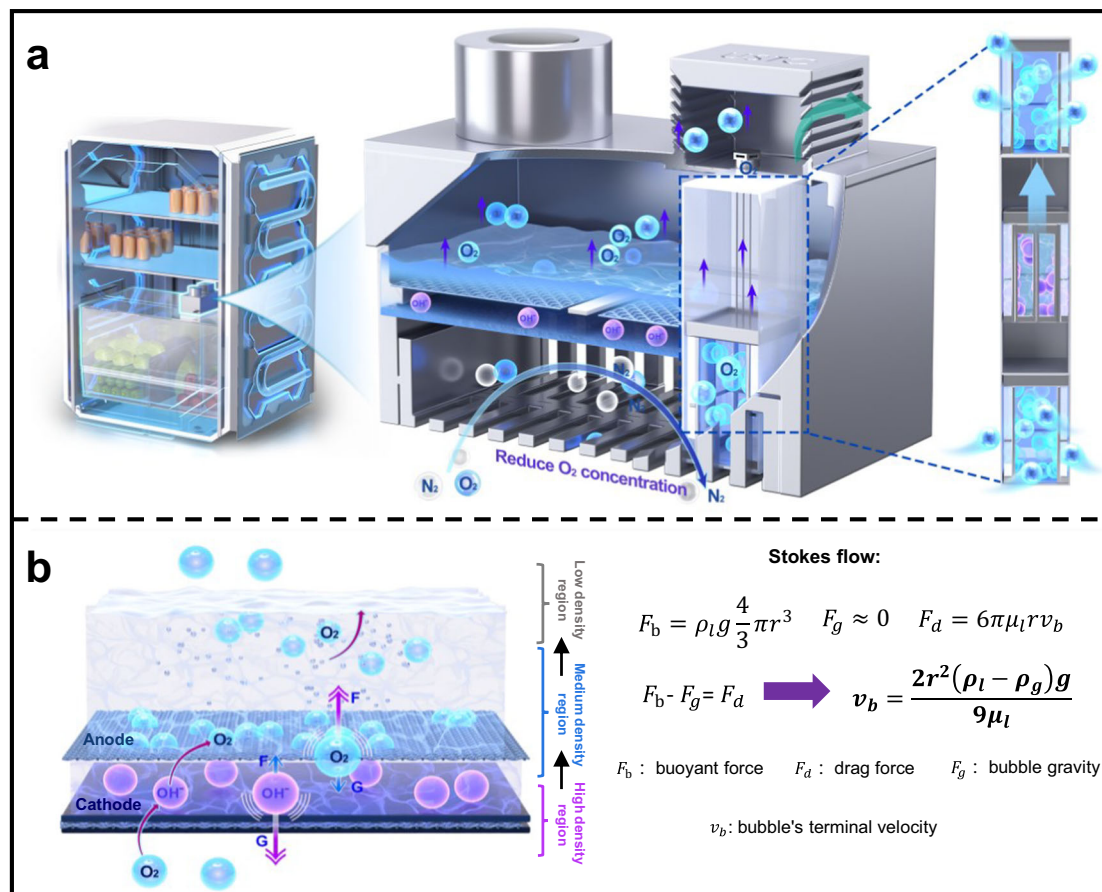


**Fig. 1** | Illustrates the gravity-assisted oxygen removal process. **a** Schematic of oxygen removal by the gravity-assisted product self-separation reactor in a refrigerator. **b** Gravity-driven product self-separation due to density differences.

develop a high-performance GDE. We first synthesized an efficient and cost-effective (Fe, Co)/N-C dual single-atom catalyst (the details are shown in Figs. S1–S15 and Table S1, S2), optimizing its active sites and structure to ensure robust ORR performance. Subsequently, the research focused on refining the GDE architecture to fully leverage the catalyst's capabilities in the GAPS system and meet the reactor's stringent requirements. Specifically, the GDE is required to exhibit high mechanical strength to withstand substantial liquid pressure, ensuring long-term operational stability; high electrochemical stability to meet the 10-year lifespan requirement for refrigerator applications; enhanced gas permeability to facilitate rapid mass transport in the ORR; and high electrical conductivity to minimize ohmic resistance, thereby optimizing overall system efficiency. These improvements aim to significantly enhance the GDE's performance in real-world applications, ensuring its sustained stability and high efficiency over extended periods of operation. In meeting these stringent requirements, polytetrafluoroethylene (PTFE) plays a pivotal role<sup>23–25</sup>. Its hydrophobicity enables precise regulation of the electrode's internal gas–liquid distribution, significantly improving gas diffusion pathways and reducing liquid-phase blockage, thereby effectively enhancing mass transfer efficiency. Its chemical inertness imparts long-term stability in corrosive environments, while its remarkable mechanical strength not only extends electrode lifespan but also preserves structural and performance reliability under external loads and sustained operational stress. These attributes make PTFE indispensable in electrode construction and GDE optimization, providing a robust foundation for achieving efficient, stable electrochemical reactions.

However, traditional carbon paper-based GDE continue to encounter considerable challenges in terms of mechanical strength

and long-term stability (Fig. 2a, b and Fig. S16). In the multilayered hierarchical fabrication process, while repeated impregnation of PTFE followed by sintering can enhance the mechanical strength and stability of the electrode, this approach is often accompanied by volumetric shrinkage and internal stresses, which in turn compromise the interfacial bonding between the microporous layer (MPL) and the carbon fiber substrate. Moreover, an excessive amount of PTFE impedes efficient electron conduction and increases interfacial resistance, leading to a reduction in reaction kinetics. Additionally, although thinner substrate layers can improve reaction performance, they simultaneously limit the mechanical strength of the electrode. These inherent structural trade-offs create significant challenges in achieving a balance between long-term stability and high performance in traditional carbon paper GDE. To gain deeper insight into these limitations, we conducted a comprehensive microstructural analysis of carbon paper GDE using high-resolution X-ray CT and SEM. The 3D CT reconstruction (Fig. 2c) clearly reveals the layered structure of the carbon paper, while SEM cross-sectional imaging (Fig. 2d) indicates an MPL thickness of ~70 μm. Elemental mapping (Fig. 2e) confirms that PTFE is highly concentrated in the MPL region, with minimal content in the carbon fiber support and catalyst layers. These findings indicate that the inherent layered design leads to uneven PTFE distribution, which is a key factor undermining the electrochemical stability of carbon paper GDE, thereby preventing catalyst-loaded carbon paper GDE from meeting the extended service life required in this study.

To address this issue, we improved the GDE fabrication and structural design to achieve uniform PTFE distribution at high loadings. By thoroughly mixing carbon spheres, a large amount of PTFE, and a suitable solvent, and then drying the mixture in an oven to form a

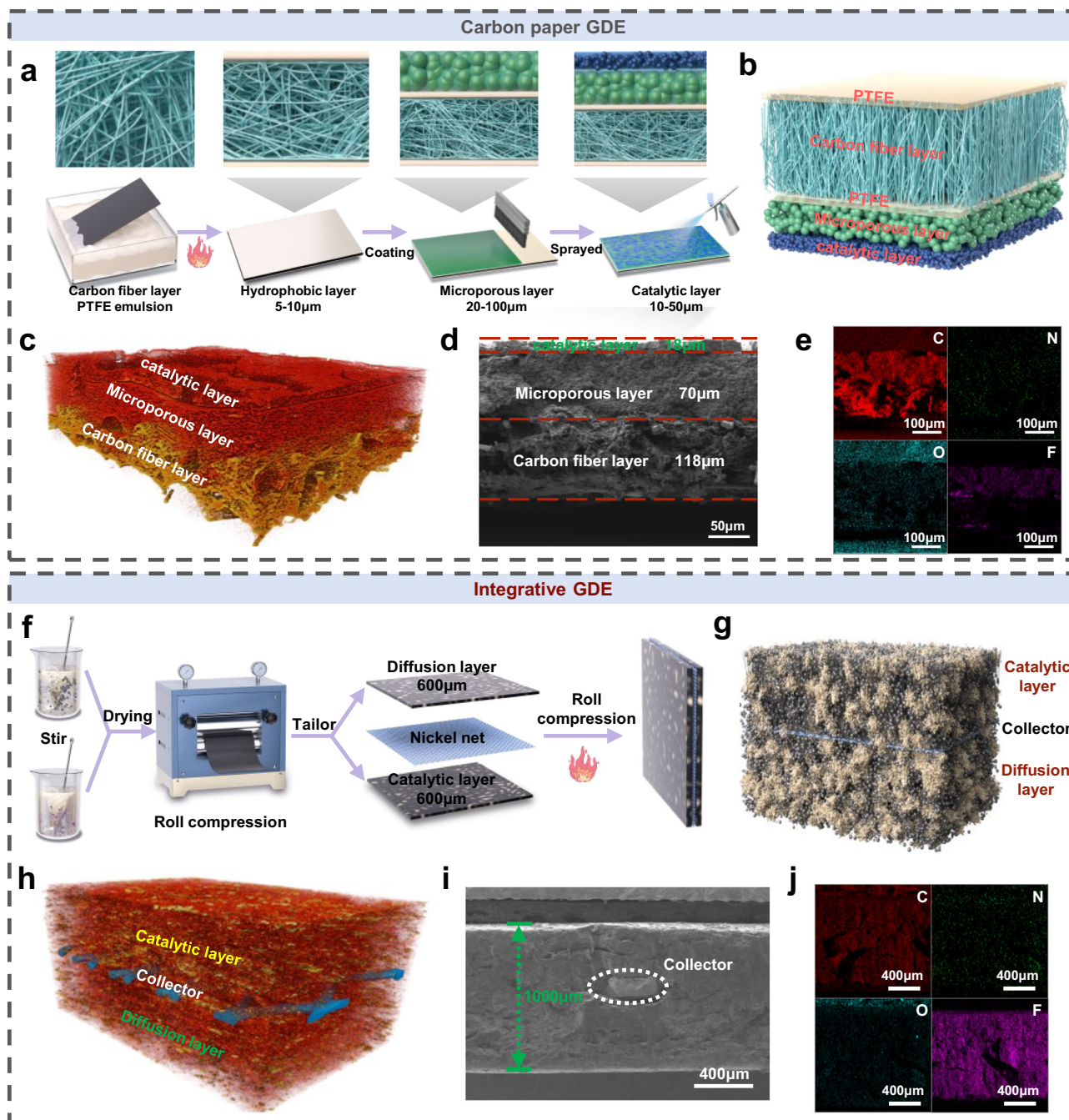


**Fig. 2 | Schematic illustration and characterization of the carbon paper gas diffusion electrode (GDE) and integrative GDE. a** Schematic illustration of the carbon paper preparation process. **b** Schematic diagram depicting the layered structure of the carbon paper. **c** High-resolution 3D CT scan reconstruction of the carbon paper. **d** Side-view SEM image of the carbon paper. **e** Elemental mapping of

the carbon paper (side view). **f** Schematic illustration of the integrative GDE preparation process. **g** Schematic diagram of the layered structure of the integrative GDE. **h** High-resolution 3D CT scan reconstruction of the integrative GDE. **i** Side-view SEM image of the integrative GDE. **j** Elemental mapping of the integrative GDE (side view).

gel-like material, we produced an integrated diffusion layer through rolling steps. The catalyst layer was fabricated using the same method, except that part of the carbon spheres was replaced with the ORR catalyst. Finally, the catalyst layer, nickel mesh, and diffusion layer were tightly pressed together and sintered, forming a robust and fully integrated GDE. The current collector, analogous to the reinforcing steel in a building structure, is embedded within the GDE, serving both structural support and electrical conduction roles, significantly enhancing the mechanical strength of the integrative GDE (Fig. 2f, g and Fig. S17). This design realized a high PTFE loading in both the diffusion layer (60%) and the catalyst layer (40%), ensuring uniform

PTFE distribution. Embedding a nickel mesh at the center of the GDE enhanced internal electron transport and reduced interfacial resistance, thereby significantly improving overall electrochemical performance. High-resolution CT and SEM analyses further confirmed the effectiveness of this optimization strategy. The 3D CT reconstruction (Fig. 2h) revealed a uniformly structured GDE with evenly distributed pores, while the SEM cross-sectional image (Fig. 2i) showed that the diffusion and catalyst layers had thicknesses of ~550 and 450 µm, respectively. Elemental mapping (Fig. 2j) clearly demonstrated uniform PTFE distribution throughout the entire electrode system.

To achieve optimal synergy between the electrode and reactor structure, we meticulously refined the electrode formulation to enhance overall performance. First, to maintain good conductivity under high PTFE loading, we introduced highly conductive carbon nanotubes (CNTs) to form an efficient conductive network<sup>26,27</sup>, thereby reducing the in-plane resistivity of the electrode. However, the addition of CNTs may weaken interlayer adhesion, leading to “slippage” at interfaces, which compromises mechanical strength and the stability of the rolling-forming process. Thus, a careful balance between conductivity and mechanical strength is required. Experimental results (Fig. 3a and Figs. S18, 19a–c) show that when the CNTs content reaches 20%, the electrode becomes difficult to form, and its mechanical strength decreases significantly to 3.69 MPa. In contrast, at 10% CNTs loading, the integrative GDE achieves a tensile strength of 12.4 MPa (the internal nickel mesh exhibits a tensile strength of up to 60 MPa), far exceeding the 5.14 MPa of traditional carbon paper, while maintaining an in-plane resistivity of  $14.3 \text{ m}\Omega \cdot \text{cm}^{-2}$ —only 10% higher than that of traditional carbon paper ( $13.0 \text{ m}\Omega \cdot \text{cm}^{-2}$ ). This finding indicates that by appropriately tuning the CNTs content, one can achieve a balance between conductivity and mechanical strength. In this study, a 10% CNTs loading was ultimately selected as the optimized formulation.

Furthermore, building on the optimization of conductivity, this study further improved the electrode’s gas permeability by incorporating ammonium bicarbonate as a pore-forming agent into the formulation<sup>28,29</sup>. Its thermal decomposition, which generates ammonia and carbon dioxide, significantly enhances the internal porosity of the electrode. However, increasing porosity can reduce material density and mechanical strength, complicating the forming process and necessitating a balance between permeability and mechanical strength. Experimental results (Fig. 3b and Figs. S19d–f–S21) show that at a 10% ammonium bicarbonate loading, the electrode becomes difficult to form, with an average pore size of  $\sim 143.21 \text{ nm}$  (4 V/A), and its mechanical strength decreases to 3.99 MPa. Ultimately, a 5% loading was selected, which maintains the integrative GDE’s overall tensile strength at 11.1 MPa, significantly surpassing the 5.14 MPa of traditional carbon paper, while enhancing the porosity to 54.3%, just 19.9% lower than the 67.7% porosity of conventional carbon paper. The average pore size is approximately  $58.87 \text{ nm}$  (4 V/A). Additionally, the in-plane resistivity is maintained at  $15.2 \text{ m}\Omega \cdot \text{cm}^{-2}$ , only 16.9% higher than the  $13.0 \text{ m}\Omega \cdot \text{cm}^{-2}$  of traditional carbon paper (Fig. S22). This combination achieves an optimized balance between conductivity, gas permeability, and mechanical strength.

Following the optimization of the electrode formulation and structure, the integrative GDE underwent a 2 V constant-voltage electrochemical stability test within a flow-cell system. The results (Fig. 3c) demonstrated that, during 100 h of continuous operation, the current density of the integrative GDE remained stable at  $-75.40 \text{ mA}\cdot\text{cm}^{-2}$ , only about 10% lower than that of the carbon paper electrode ( $83.25 \text{ mA}\cdot\text{cm}^{-2}$ ), with no observable current decay. Furthermore, the contact angle of the electrode surface only slightly decreased from  $122.3^\circ$  to  $117.1^\circ$ , indicating exceptional catalytic activity and electrochemical stability. In stark contrast, the carbon paper electrode exhibited considerable current decay after only 20 h of operation, with its contact angle plummeting from  $126.5^\circ$  to  $48.3^\circ$ , signaling poor long-term stability. The integrative GDE strikes a balance between conductivity, gas permeability, mechanical strength, electrochemical stability, and cost (Fig. 3d). To further investigate the cause of performance degradation in the carbon paper electrode, infrared (IR) and Raman spectroscopy analyses were performed before and after the reaction (Fig. 3e). These analyses revealed a substantial increase in oxygen-containing functional groups and carbon-carbon double bonds on the surface of the carbon paper post-reaction. The  $I_{\text{D}}/I_{\text{G}}$  ratio showed a marked increase, further confirming corrosion and structural degradation of the carbon-based material. X-ray photoelectron

spectroscopy (XPS) results also indicated a significant rise in oxygen-containing groups on the carbon paper electrode surface, coupled with the degradation of PTFE, leading to a notable decrease in hydrophobicity, which correlated with the observed performance deterioration. In stark contrast, the integrative GDE retained its stable microstructure even after prolonged electrochemical reaction (Fig. 3f). IR and Raman spectroscopy analyses showed no significant accumulation of oxygen-containing functional groups or formation of carbon-carbon double bonds, with the  $I_{\text{D}}/I_{\text{G}}$  ratio remaining almost unchanged, indicating minimal oxidation or structural degradation. XPS analysis further confirmed that the chemical states of the elements on the surface of the integrative GDE remained virtually unchanged before and after the reaction. This further emphasizes the remarkable electrochemical stability of the integrative GDE. These results ensure that the integrative GDE maintains exceptional structural stability and consistently delivers high electrochemical performance under elevated liquid pressure conditions, fully meeting the stringent requirements for long-term stability and high efficiency in the GAPS system.

In EOR systems, the theoretical electrochemical rate (TER) and product separation efficiency (PSE, Fig. 4a) are two critical parameters for performance evaluation. TER characterizes the maximum achievable reaction rate of the system under specific conditions, while PSE measures the effectiveness of separating cathodic and anodic products. TER can be expressed as:

$$\text{TER} = \frac{I_{\text{max}}}{nF} \quad (6)$$

where  $I_{\text{max}}$  is the maximum achievable current under given conditions,  $n$  is the number of electrons transferred per reaction, and  $F$  is the Faraday constant.

In this study,  $\text{O}_2$  serves both as the cathodic reactant and the anodic product. Therefore, achieving a high TER while effectively preventing anodically generated  $\text{O}_2$  from diffusing to the cathode and undergoing self-consumption (i.e., enhancing PSE) is crucial for improving  $\text{O}_2$  removal efficiency and current utilization. We further evaluated the system’s operational performance and feasibility under practical application conditions. We first examined the impact of the anode-cathode spacing on TER and PSE: decreasing the spacing increases reaction rate but raises the risk of  $\text{O}_2$  back-diffusion, while increasing the spacing reduces back-diffusion but lowers the reaction rate, both affecting actual  $\text{O}_2$  removal performance. Through constant-voltage testing at 2 V on a  $4 \text{ cm}^2$  micro GAPS Reactor (Fig. 4b, c and Fig. S23), the results demonstrate that as the anode-cathode distance increases, the current density of the reactor progressively declines, while the  $\text{O}_2$  removal time exhibits an initial decrease followed by an increase. At a 3 mm anode-cathode distance, the current density reaches  $96.5 \text{ mA}\cdot\text{cm}^{-2}$  (slightly lower than  $118.7 \text{ mA}\cdot\text{cm}^{-2}$  at 1 mm and higher than  $82.7 \text{ mA}\cdot\text{cm}^{-2}$  at 6 mm), yielding the most rapid  $\text{O}_2$  removal rate, reducing the  $\text{O}_2$  concentration in a 0.5 L sealed chamber to 10% within 27 min (faster than 30.6 min at 1 mm and 31.2 min at 6 mm). High-speed imaging results show that the bubble radius is approximately 0.1 mm, with an ascent velocity of about  $0.048 \text{ m}\cdot\text{s}^{-1}$  (Fig. S24). Further simulation analysis (Fig. 4d, e and Table S3) incorporated the physical mechanisms underlying  $\text{O}_2$  distribution and movement, specifically the diffusion characteristics of  $\text{O}_2$  in the liquid phase and the effects of buoyancy. Due to the density difference between  $\text{O}_2$  and the solution,  $\text{O}_2$  predominantly rises in the vertical direction under buoyant forces, the uniformity test results indicate that the bubble distribution during  $\text{O}_2$  rise is highly uniform, with a uniformity of approximately 94%. However, in the anode region, a concentration gradient generated by  $\text{O}_2$  evolution leads to some  $\text{O}_2$  diffusing downward toward the cathode region. This effect is more pronounced at smaller anode-cathode distances (e.g., 1 mm), as it facilitates the diffusion of  $\text{O}_2$  to the cathode, where it is self-consumed, thereby

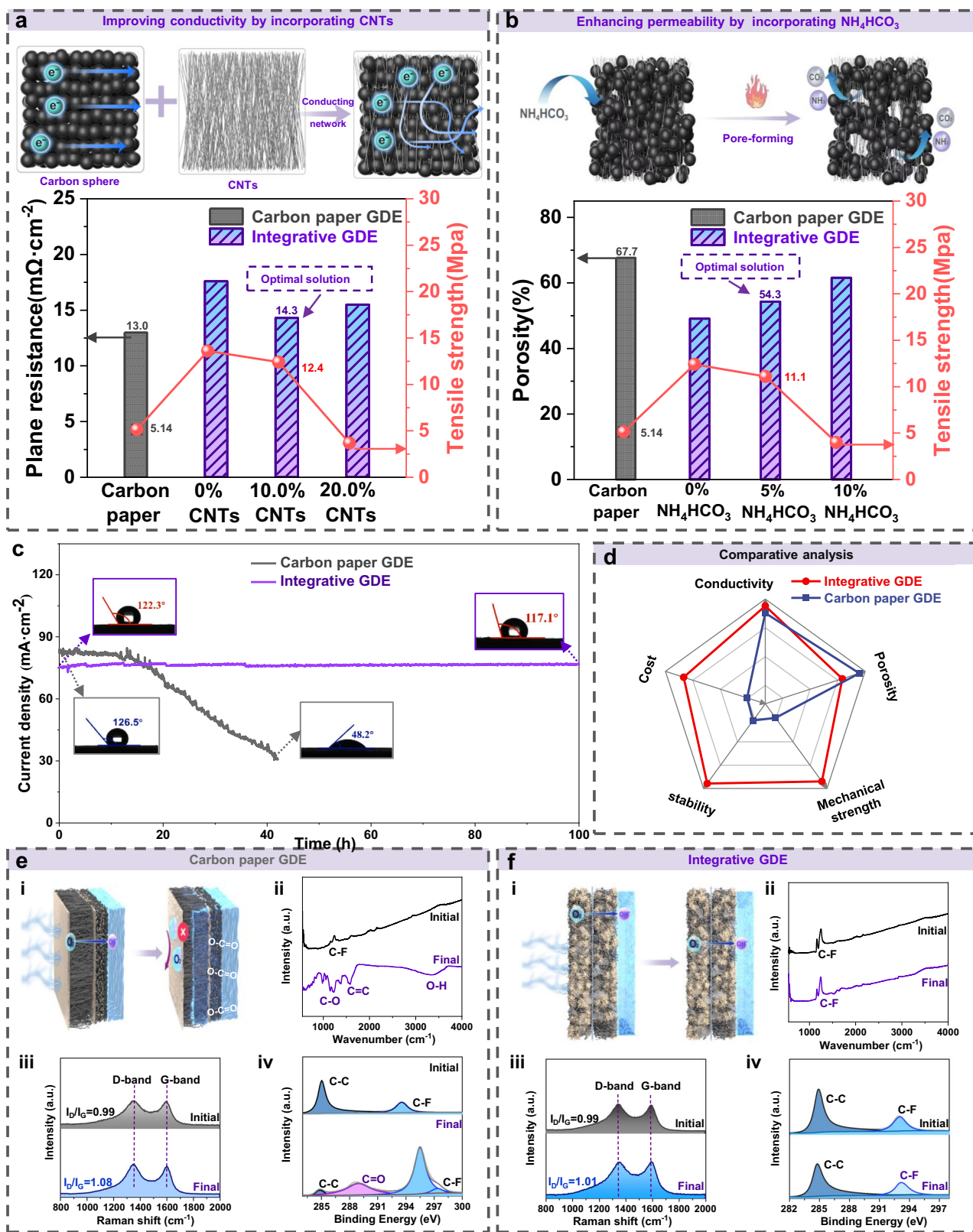


**Fig. 3 | Structural and performance optimization of integrative gas diffusion electrode (GDE).** **a** Conductivity enhancement and mechanical strength testing of integrative GDE with varying carbon nanotube contents. **b** Gas permeability improvement and mechanical strength testing of integrative GDE with different ammonium bicarbonate contents. **c** Stability and contact angle measurements for carbon paper and integrative GDE. **d** Radar chart comparing the performance parameters of carbon paper GDE and integrative GDE. **e** Stability of carbon paper

before and after reaction: (i) Schematic illustration, (ii) Infrared spectroscopy, (iii) Raman spectroscopy, (iv) X-ray photoelectron spectroscopy analysis. **f** Stability of integrative GDE before and after reaction: (i) Schematic illustration, (ii) Infrared spectroscopy, (iii) Raman spectroscopy, (iv) X-ray photoelectron spectroscopy analysis. Source data for Fig. 3a–f are provided as a Source Data file.

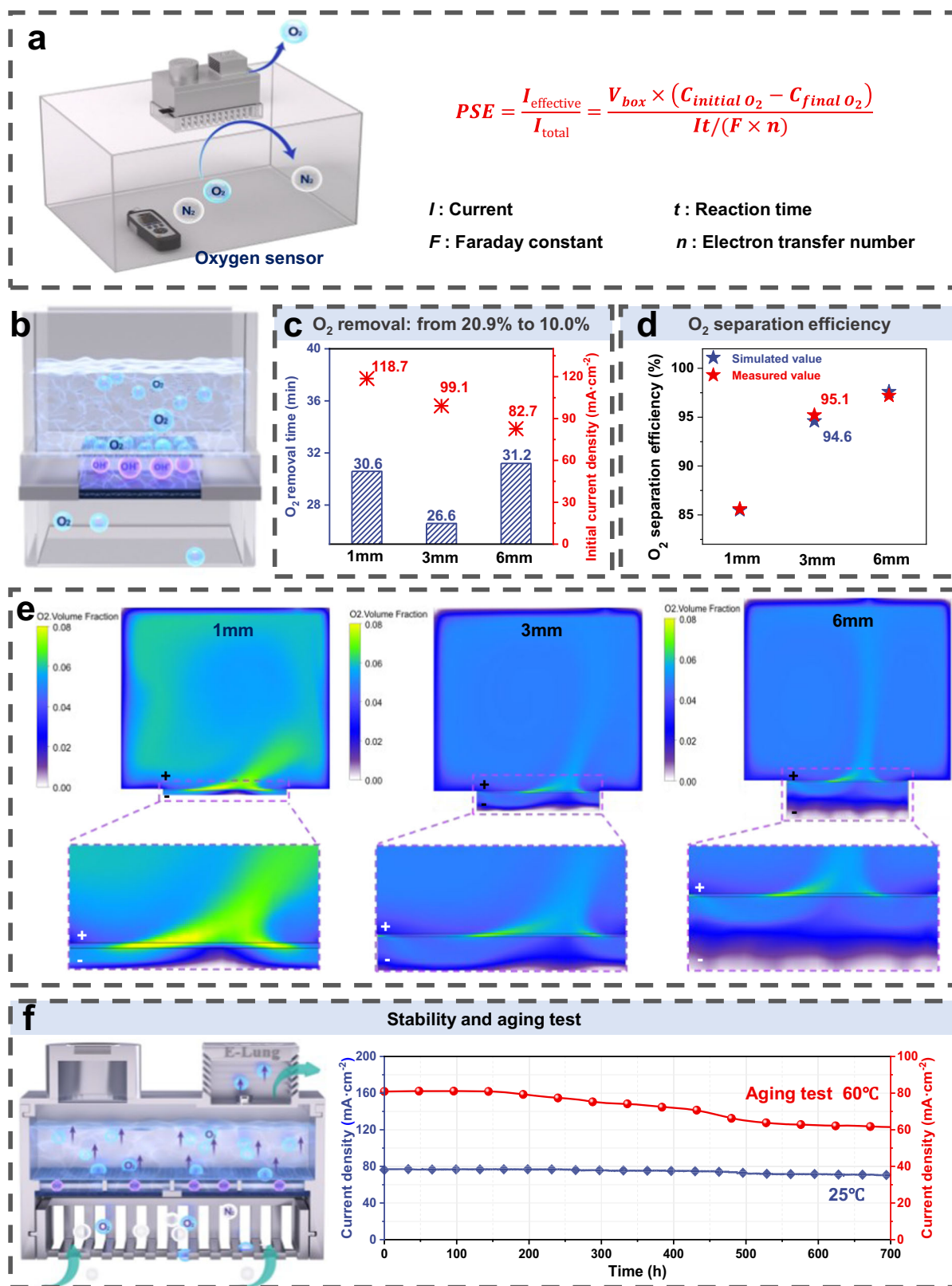


**Fig. 4 | Performance evaluation and design of the gravity-assisted product self-separation (GAPS) Reactor.** **a** Separation efficiency of anode and cathode products. **b** Schematic of the 4 cm<sup>2</sup> micro GAPS Reactor. **c** Initial current density and oxygen (O<sub>2</sub>) removal time of the micro GAPS Reactor. **d** Comparison of measured

and simulated O<sub>2</sub> separation efficiencies at various electrode spacings. **e** Simulation of O<sub>2</sub> separation efficiency at different electrode spacings. **f** Schematic of the 50 cm<sup>2</sup> GAPS Reactor, along with stability and aging performance tests of the GAPS Reactor. Source data for Fig. 4c, d, f are provided as a Source Data file.

reducing the separation efficiency. As the anode-cathode distance increases, O<sub>2</sub> diffusion is increasingly restricted by the larger spatial volume, and the downward diffusion to the cathode diminishes, leading to reduced O<sub>2</sub> self-consumption at the cathode. The simulation results are consistent with experimental data. At a 1 mm anode-cathode distance, the O<sub>2</sub> concentration between the anode and cathode is relatively high, indicating significant self-recirculation of O<sub>2</sub>. This self-recirculation leads to some O<sub>2</sub> diffusing towards the cathode, where it undergoes self-consumption in the ORR, thereby reducing the overall separation efficiency. The simulated separation efficiency at this distance is 85.5% (measured value: 85.6%). In contrast, at 3 and 6 mm distances, the overall O<sub>2</sub> concentration between the anode and cathode is significantly lower, suggesting that the self-recirculation effect is minimized. As a result, a larger proportion of O<sub>2</sub> diffuses directly to the exterior, rather than being consumed at the cathode, leading to a significant improvement in separation efficiency. At a 3 mm distance, the simulated separation efficiency reaches 94.6% (measured value: 95.1%), while at 6 mm, it increases to 97.6% (measured value: 97.2%). This behavior suggests that both buoyancy effects and concentration gradients interact synergistically to optimize O<sub>2</sub> separation efficiency. Although the separation efficiencies at 3 and 6 mm are similar, the current density at 3 mm is 16.7% higher than at 6 mm, and the O<sub>2</sub> removal performance at 3 mm is superior. After considering the trade-off between reaction rate and O<sub>2</sub> separation efficiency, a 3 mm anode-cathode distance was identified as the optimal configuration. Furthermore, we conducted further analysis and optimization of the module components to determine the optimal module structure (Figs. S25–S31).

To meet the practical requirements of refrigerators, we adopted a large-area open cathode design, expanding the electrode area to 50 cm<sup>2</sup> to compensate for the lack of a gas–liquid circulation system (Fig. 4f and Fig. S32). This design enhances O<sub>2</sub> diffusion efficiency and improves the mass transfer process, effectively overcoming the limitations typically associated with the absence of a circulation system (Figs. S33, S34): the time required to reduce the O<sub>2</sub> concentration in a 20 L sealed chamber to 10% increased by only 2.3% compared to a conventional gas circulation design (210 min vs. 205 min), these results indicate that the large-area open cathode design effectively mitigates mass transfer limitations, while energy consumption decreased by 30%. At 5 °C, the same O<sub>2</sub> removal efficiency was achieved within 270 min (Fig. S35), and no hydrogen was detected at voltages below 2.2 V (Fig. S36), ensuring both efficiency and safety in refrigerator applications. Moreover, the reactor's polypropylene +30% glass fiber construction guarantees human safety. Long-term stability tests showed that performance declined by only 8.2% after 700 h of continuous operation at 25 °C. The module is designed for a service life of 10 years, with a total of 43,800 h based on 10 h of daily operation. Given the impracticality of conducting long-term testing, we apply the Arrhenius model, which establishes a relationship between high-temperature aging and performance at operating temperatures. This well-established model for material aging and device failure uses activation energy to determine an acceleration factor, facilitating the extrapolation of the module's lifespan under typical operating conditions.

$$Af_{(T)} = \exp\left\{\frac{E_a}{R}\left(\frac{1}{T_1} - \frac{1}{T_2}\right)\right\} \quad (7)$$

The activation energy is  $E_a = 0.6$  eV, the Boltzmann constant is  $R = 8.617 \times 10^{-5}$  eV·K<sup>-1</sup>, with the operating temperature at 5 °C ( $T_1 = 278$  K), and the accelerated testing temperature at 60 °C ( $T_2 = 333$  K). Using these values, the Arrhenius acceleration factor  $Af_{(60\text{ }^\circ\text{C})}$  is calculated to be 62.60. Therefore:

$$\frac{43800}{62.60} \approx 700 \text{ (hours)} \quad (8)$$

Using an Arrhenius-based acceleration model, the higher-temperature (60 °C) test data were mapped to normal-use conditions, indicating that 700 h at 60 °C equates to roughly 10 years of operation at a lower temperature (5 °C). The results of the 60 °C aging test show a performance degradation of less than 25% after 700 h, validating the reactor's expected 10-year service life. This approach demonstrates that the minimal decay under accelerated tests reliably predicts long-term durability and performance, meeting refrigerator industry standards. In addition, consistent O<sub>2</sub> removal times across different batches (Fig. S37) confirmed the design's reproducibility and potential for large-scale production. In summary, the single-cell 50 cm<sup>2</sup> GAPS Reactor achieves a balance between performance and lifespan. Furthermore, removing metal plates, ion-exchange membranes, and gas–liquid circulation components significantly reduces the reactor's cost. Increasing the electrode area further is expected to continue improving performance, indicating that the membrane-free, self-separating electrochemical O<sub>2</sub> removal reactor proposed in this study holds substantial promise for household refrigerator preservation applications.

Building on the comprehensive balance of performance, cost, and lifespan achieved by the single-cell reactor, we further explored reactor integration and operational strategies tailored to actual refrigerator conditions. Although increasing the electrode area of a single-cell reactor can boost O<sub>2</sub> removal rates, it may cause the current to exceed the refrigerator's electrical control threshold, leading to excessive heat load, energy losses, and reduced overall stability. To overcome this limitation, we regulated the relationship between electrode area and current density and proposed a series-connected anode-cathode integration strategy. This approach strictly controls the current while significantly enhancing O<sub>2</sub> removal efficiency, thereby enabling high-efficiency O<sub>2</sub> removal under the refrigerator's existing electrical constraints. Based on this strategy, we integrated two 50 cm<sup>2</sup> integrative GDE into a two-cell series-connected configuration within a single-cell reactor and tested it under real refrigerator conditions. In this design, the cathode end is embedded into the storage drawer, allowing O<sub>2</sub> in the drawer to freely diffuse to the cathode interface for efficient ORR-based removal; simultaneously, O<sub>2</sub> generated at the anode is released through a top vent, preventing self-consumption due to O<sub>2</sub> back-diffusion (Fig. 5a). Experimental results show that under 3 A constant current and 4 V operating conditions, the two-cell series-connected reactor can reduce the O<sub>2</sub> concentration in a 20 L storage drawer to 10% within 155 min, with power consumption below 12 W and a single-cycle O<sub>2</sub> removal energy consumption of less than 0.031 kWh, all while maintaining stable temperature and humidity in the drawer (Fig. 5b–d). Further safety tests show that no hydrogen is generated during normal operation of the reactor (Fig. S38 and Table S4). Even under fault conditions (10 A constant current for 6 h), the hydrogen concentration in the drawer remains below 600 ppm (Table S5), well below the safety threshold, ensuring long-term operational safety. Moreover, the two-cell series-connected reactor displays exceptional low-temperature durability, with performance decreasing by only 11.1% after 600 h of continuous operation at 5 °C (Fig. 5e). High-frequency door opening and closing tests simulating user scenarios (20 times per day, each for 120 s) confirm that the system can rapidly return to the initial O<sub>2</sub> level within 100 s after the door is opened (Fig. S39), and 30-day dynamic tests show no significant change in the time required to reduce drawer O<sub>2</sub> concentration to 10% (Fig. 5f), demonstrating robust adaptability and stability under realistic household conditions. Food preservation tests further verify the reactor's practical value: compared to lettuce that rots within 5 days at room temperature or shows obvious spoilage within 10 days in a conventional refrigerator, lettuce stored in the refrigerator equipped with this low-O<sub>2</sub> reactor only exhibits mild deterioration at 30 days (Fig. 5g). Vitamin C analysis provides additional evidence of nutrient retention under low-temperature,

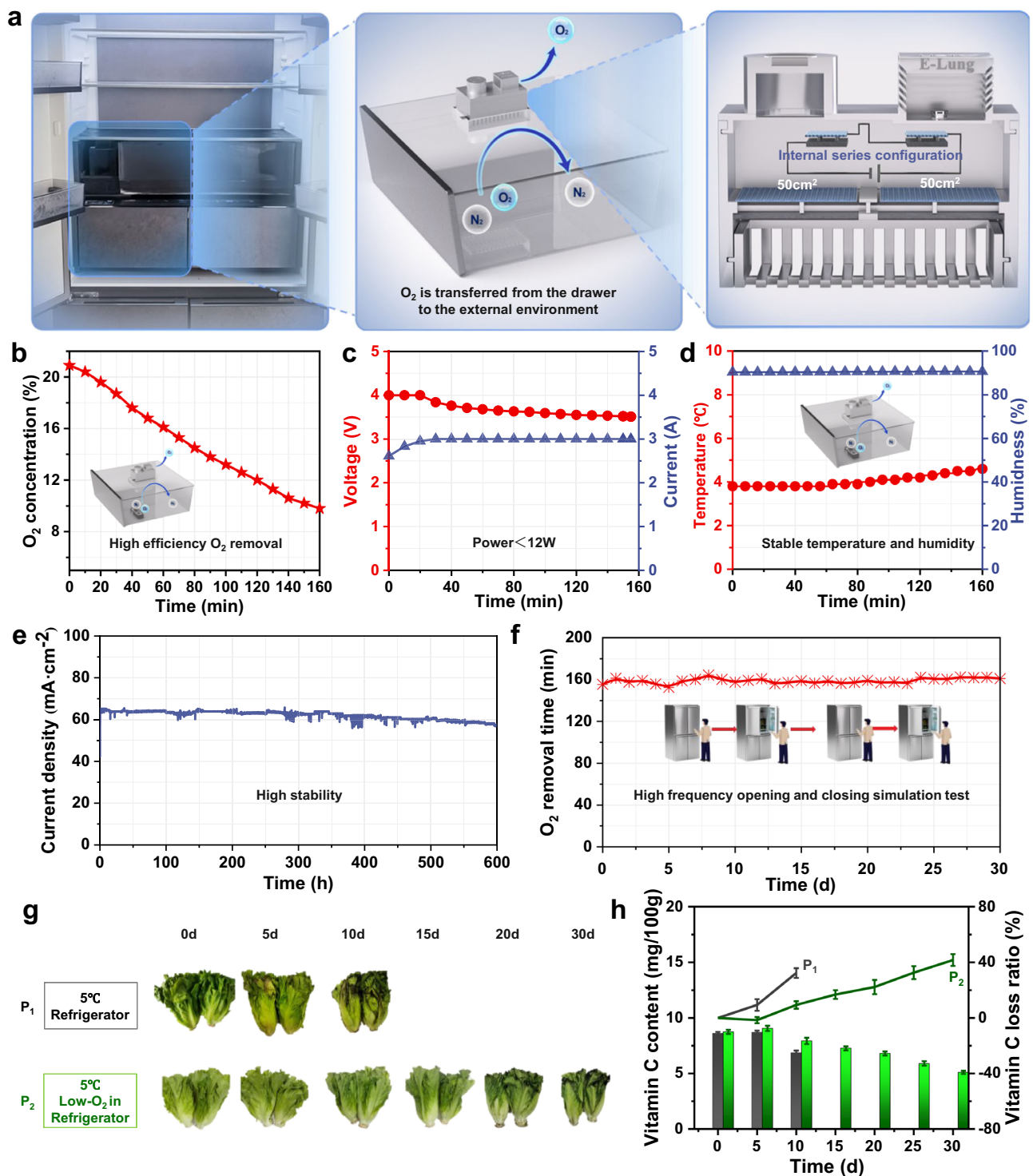


**Fig. 5 | Performance and evaluation of the two-cell series-connected reactor integrated into a refrigeration system for food preservation.** **a** Schematic diagram of the two-cell series-connected gravity-assisted product self-separation (GAPS) Reactor integrated into the refrigeration system, illustrating the drawer connection and internal structure. **b** Oxygen (O<sub>2</sub>) removal performance of the two-cell series-connected reactor under refrigeration conditions. **c** Voltage and current fluctuations during O<sub>2</sub> removal. **d** Temperature and humidity variations during O<sub>2</sub>

removal. **e** Stability test of the reactor at 4 V under refrigeration conditions. **f** O<sub>2</sub> removal time under conditions of frequent door openings. **g** Comparison of lettuce freshness stored in a conventional refrigerator, and in a low-O<sub>2</sub> reactor-equipped refrigerator. **h** Vitamin C retention under different storage conditions (Error bars represent the standard error of the mean from three independent tests). Source data for Fig. 5b–f, h are provided as a Source Data file.

low-O<sub>2</sub> conditions: after 10 days, the vitamin C loss rate in a conventional refrigerator is 3.46 times that in the low-O<sub>2</sub> environment (Fig. 5h), highlighting the unique advantage of the low-O<sub>2</sub> coupling strategy in food preservation.

After successfully demonstrating efficient and stable low-O<sub>2</sub> storage using the two-cell series-connected reactor under actual refrigerator conditions, this study further assessed its economic feasibility and commercial potential through a comprehensive

comparison with a conventional two-cell series-connected ion-exchange membrane-based electrochemical O<sub>2</sub> removal (IEM-based EOR) reactor, thereby providing quantitative guidance for large-scale commercial implementation. The results show that through systematic optimization of catalysts, electrodes, and reactor structures, our GAPS Reactor is significantly more cost-effective and durable than a traditional IEM-based EOR reactor. Cost analysis indicates that, for the same electrode area, the total cost of a conventional two-cell series-connected IEM-based EOR reactor reaches USD 433.1 (Fig. 6a, b and Tables S6–S8), whereas our GAPS Reactor costs only USD 7.411—less than 1.7% of the IEM-based EOR reactor's cost—revealing a tremendous cost advantage (The cost of the electrode assembly is relatively reduced by 97.6%, the cost of device fittings is relatively reduced by 98.2%, and there is no cost associated with the gas–liquid circulation system). Although the IEM-based EOR's O<sub>2</sub> removal rate is ~2.5 times higher than that of our reactor (Fig. S40), when normalized by cost, the IEM-based EOR's rate is only 0.0838 ml·min<sup>-1</sup>·USD<sup>-1</sup>, far lower than our reactor's 1.897 ml·min<sup>-1</sup>·USD<sup>-1</sup> (Fig. 6c), highlighting the superior balance of performance and cost achieved by our design. Beyond economic benefits, this reactor also offers exceptional longevity and minimal maintenance requirements. Under no-maintenance conditions, its ser-

vice life reaches up to 10 years, whereas the IEM-based EOR reactor demands one maintenance session per year to extend its service life, which increases operational costs and compromises user experience. Additionally, it exhibits a slight advantage in energy consumption (0.014 kWh per liter O<sub>2</sub> removed, compared to 0.016 kWh for the IEM-based EOR). These strongly demonstrate that the GAPS reactor exhibits high O<sub>2</sub> removal efficiency.

GAPS Reactor's primary economic advantage lies in its design, which requires no additional components and is virtually maintenance-free—resulting in a total cost of ownership (TCO) of just USD 7.411 over a 10-year lifespan at a 5% discount rate (*r*) (Fig. 6d), with no further expenses once installed. Since no annual replacement or repairs are needed, any household refrigerator whose profit margin exceeds USD 7.411 can profitably integrate the GAPS Reactor. Moreover, because of its small footprint (~1L) and simple structure, the GAPS Reactor can be seamlessly incorporated into existing refrigeration designs. In mid-to high-end models, this single upfront investment—in tandem with “zero” ongoing costs and superior freshness preservation—can significantly strengthen the refrigerator's competitive positioning and price premium. By contrast, the IEM-based EOR module requires one maintenance operation annually, each amounting to ~30% of the module's cost<sup>30,31</sup>. Consequently, its

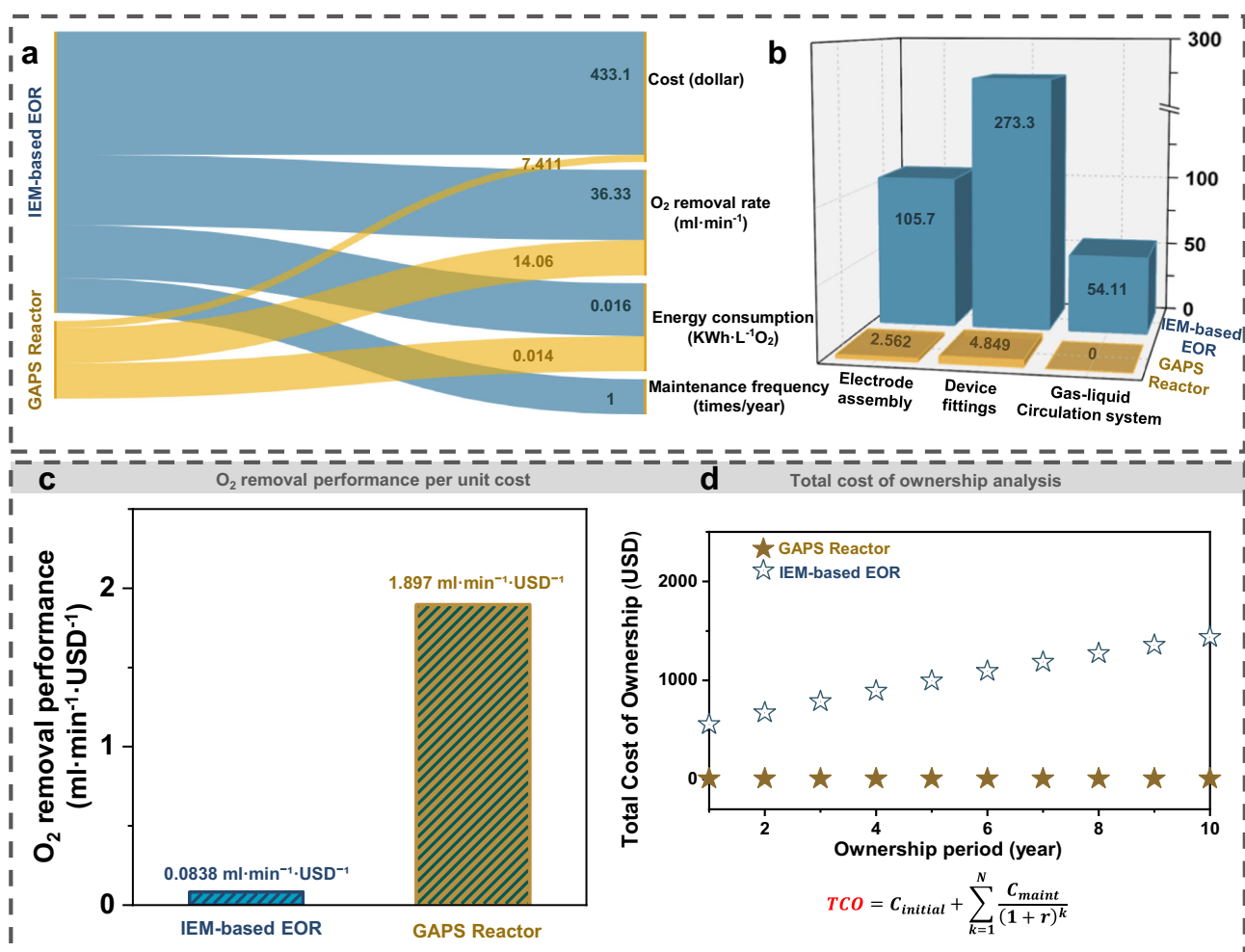


**Fig. 6** | Performance and cost comparison of the ion-exchange membrane-based electrochemical Oxygen removal (IEM-based EOR) reactor and the gravity-assisted product self-separation (GAPS) Reactor. **a** Comparison of key parameters between the IEM-based EOR reactor and the GAPS Reactor. **b** Cost comparison between the IEM-based EOR reactor and the GAPS Reactor. **c** O<sub>2</sub>

removal rate per unit equipment cost for the IEM-based EOR reactor and the GAPS Reactor. **d** The comparison of total cost of ownership over time for two O<sub>2</sub> removal modules integrated into a refrigeration system. Source data for Fig. 6a–d are provided as a Source Data file.

aggregated 10-year discounted cost reaches:

$$\text{TCO}_{\text{IEM}} = 433.1 + \sum_{k=1}^{10} \frac{433.1 \times 30\%}{(1 + 0.05)^k} = 1436.4 \text{ USD} \quad (9)$$

This TCO far exceeds the USD 7.411 for the GAPS Reactor. Manufacturers must therefore maintain a profit margin substantially above USD 1436.4 per unit to avoid a net loss, a target that is clearly unrealistic for most consumer-grade appliances. Although the IEM-based EOR module may slightly enhance O<sub>2</sub> removal rates, its prohibitive replacement and maintenance expenses restrict its application to only a handful of ultra-premium or specialized markets. In contrast, GAPS Reactor's lack of auxiliary parts, maintenance-free operation, and minimal volume not only unlock substantial returns in mid- to high-end refrigerators but also provide a technologically and economically advantageous foundation for further extension into food packaging, pharmaceutical storage, and other low-O<sub>2</sub> applications. This outcome aligns with the era's emphasis on green transformation and technological advancement, providing robust support for the widespread promotion of next-generation, cost-effective electrochemical O<sub>2</sub> removal technologies.

## Discussion

This study introduces a GAPS reactor that eliminates costly ion-exchange membranes and auxiliary circulation, leveraging natural density differences to achieve up to 95% product self-separation without forced flow. An integrative GDE offers 2.2-fold higher mechanical strength and 30-fold greater stability than conventional carbon paper, supporting robust, decade-long operation under elevated hydrostatic pressure. In a two-cell series configuration within refrigerators, the reactor boosts fresh-keeping capacity by 3.4-fold. Economic analysis further demonstrates a 22.6-fold improvement in cost-effectiveness over IEM-based EOR. Collectively, this work establishes a practical, long-lived blueprint for next-generation electrochemical O<sub>2</sub> removal with broad consumer and industrial impact.

## Methods

### Chemicals

Nitric acid (HNO<sub>3</sub>), FeCl<sub>3</sub>, CoCl<sub>2</sub>·6H<sub>2</sub>O, ethanol, potassium hydroxide (KOH), ammonium bicarbonate (NH<sub>4</sub>HCO<sub>3</sub>), and melamine were obtained from Sinopharm Chemical Reagents (China). Nafion solution (5 wt%) was purchased from Aldrich. Pt/C (20 wt%) was supplied by Johnson Matthey (JM). Carbon black, carbon nanotubes and polytetrafluoroethylene emulsion were purchased from Alfa Aesar. All chemicals used in this study were analytical grade and were directly used without further purification. Deionized (DI) water from the Milli-Q System (Millipore, Billerica, MA) was used in all experiments.

### Synthesis

**Synthesis of oxidized carbon black (O-C).** For a typical synthesis, 5 g of carbon black was added to 300 mL of 4 M nitric acid solution and stirred vigorously at 80 °C for 8 h. After cooling, the mixture was filtered and washed with deionized water until neutral, then dried at 60 °C for 12 h.

**Synthesis of (Fe, Co)/N-C, Fe/N-C, and Co/N-C.** For a typical synthesis, 500 mg of O-C was added to a mixture of 100 mL deionized water and ethanol (1:4) and dispersed using ultrasonic treatment to form a suspension. Then, 7.5 mg of FeCl<sub>3</sub> and 12 mg of CoCl<sub>2</sub>·6H<sub>2</sub>O were dissolved in 10 mL of deionized water. This solution was added dropwise to the vigorously stirred carbon black suspension at 85 °C at a rate of 1.0 mL/min using a micro-injection pump. After the complete addition, the mixture was continuously stirred until no liquid remained. The resulting catalyst precursor was then thoroughly mixed and ground with melamine at a mass ratio of 1:10, followed by heating at

800 °C under a nitrogen atmosphere for 2 h, with a heating rate of 5 °C/min. Finally, the particles were removed by acid leaching to form (Fe, Co)/N-C. The synthesis procedures for Fe/N-C and Co/N-C are similar to that of (Fe, Co)/N-C, with only the respective metal added during synthesis, and the amount doubled.

### Preparation of integrative GDE

The catalyst, carbon black, carbon nanotubes, NH<sub>4</sub>HCO<sub>3</sub>, and PTFE emulsion were mixed in a specific proportion and stirred in a 60 °C water bath for 15 min. An appropriate amount of aqueous solution was then added, and the mixture was stirred for an additional hour to obtain a black wet slurry. After drying, the slurry formed a gel-like substance, which was then pressed with a bi-directional roller to achieve a catalytic layer thickness of 0.55 mm. Similarly, carbon black, NH<sub>4</sub>HCO<sub>3</sub>, and PTFE emulsion were mixed and pressed to form a diffusion layer of the same thickness. The catalytic layer, punched nickel mesh, and diffusion layer were then hot-pressed at 80 °C and dried overnight. The resulting semi-finished three-in-one integrative GDE was soaked in water at 60 °C for 12 h, followed by vacuum drying at 60 °C and hot-sintering at 340 °C for 1 h to produce the final integrative GDE.

### Characterization

Transmission electron microscopy (TEM) was performed on a Hitachi-7700 microscope with an acceleration voltage of 100 kV. High-resolution TEM (HRTEM), high-angle annular dark-field scanning transmission electron microscopy (HAADF-STEM), and energy-dispersive X-ray spectroscopy (EDS) elemental mapping were carried out using a JEM-2100F microscope. Aberration-corrected HAADF-STEM images were obtained on a Titan Cubed Themis G2 300. Powder X-ray diffraction (XRD) patterns were recorded using a Rigaku Mini-flex600 at 40 kV and 15 mA with Cu Kα radiation (λ = 0.15406 nm). The Brunauer–Emmett–Teller (BET) specific surface area measurements were conducted using a Micromeritics Tristar II 3020 M, with samples degassed at 300 °C for 3 h. X-ray photoelectron spectroscopy (XPS) was conducted using a Thermo Scientific ESCALAB 250Xi with Al Kα radiation, with the C1s peak at 284.8 eV as a reference. Inductively coupled plasma atomic emission spectroscopy (ICP-AES) measurements were performed using a Thermo Fisher iCAP 7400 to determine Fe and Co contents. X-ray absorption fine structure (XAFS) spectra at the Fe K-edge and Co K-edge were obtained at the IWIB station of the Beijing Synchrotron Radiation Facility (BSRF).

### Electrochemical measurements

The electrocatalytic ORR performance was evaluated using a CHI-760E electrochemical station at room temperature with a conventional three-electrode system. All potentials were measured against an Ag/AgCl reference electrode (saturated KCl, obtained from Tjaida and stored in a saturated KCl solution before use) and converted to the reversible hydrogen electrode (RHE) scale by the following equation:

$$E(\text{vs. RHE}) = E(\text{vs. Ag/AgCl}) + 0.197 \text{ V} + 0.059 \times \text{pH}$$

For catalyst preparation, 5 mg of the catalyst was dispersed in 1 mL of a 1:1 (v/v) ethanol/water mixed solvent, followed by the addition of 40 μL of 5 wt% Nafion solution. This mixture was sonicated for at least 40 min to form a homogeneous ink. For the ORR test, 10 μL of the catalyst ink was dropped onto a glassy carbon electrode (with a disc area of 0.1963 cm<sup>2</sup>) and dried to form a uniform thin film. Before measurements, nitrogen or O<sub>2</sub> gas was bubbled through the electrolyte for 30 min to obtain a nitrogen- or oxygen-saturated solution. Linear sweep voltammetry (LSV) curves were recorded in O<sub>2</sub>-saturated 0.1 M KOH at room temperature with a sweep rate of 10 mV·s<sup>-1</sup>.

### High temperature acceleration measurements

In the aging test, the reactor is loaded with 20% concentration of electrolyte, and the electrolyte volume accounts for 50% of the effective volume of the reactor. The test conditions were ambient temperature ( $60 \pm 2$ ) °C and humidity ( $90 \pm 5$ )%. After the reactor is connected to the power, the timer starts and stops after 30 days of continuous work.

### Experiment on the preservation of lettuce

This experiment aims to evaluate the application of the electrochemical O<sub>2</sub> removal reactor in food preservation. Fresh lettuce was selected as the experimental sample and divided into three groups for comparison: room temperature, conventional refrigeration, and conventional refrigeration equipped with the GAPS Reactor. The temperature in all refrigerators was set to 5 °C. During the testing period, samples were taken every 5 days, and the appearance of the lettuce leaves was recorded. Vitamin C content changes in the lettuce were quantitatively analyzed using spectrophotometry.

### Bubble rise velocity

At terminal velocity, the buoyant force (minus the bubble's own weight) balances the viscous drag:

$$F_b - F_g = F_d$$

1. Buoyant force  $F_b$ :

$$F_b = \rho_l g \frac{4}{3} \pi r^3$$

where  $g$  is the gravitational acceleration  $\approx 9.81 \text{ m}\cdot\text{s}^{-2}$ . If the bubble density ( $\rho_g$ ) is much smaller than  $\rho_l$ , the bubble's weight  $F_g$ , can often be neglected or included by using  $(\rho_l - \rho_g)$ .

2. Viscous drag  $F_d$ : under Stokes flow, a sphere of radius  $r$  moving at velocity  $v_b$  through a fluid of viscosity  $\mu_l$  experiences a drag of

$$F_d = 6\pi\mu_l r v_b$$

Neglecting  $\rho_g$  (or treating it as  $\rho_l - \rho_g$  if higher accuracy is needed), we have:

$$\rho_l g \frac{4}{3} \pi r^3 = 6\pi\mu_l r v_b$$

which can be rearranged to give the bubble's terminal velocity  $v_b$ :

$$v_b = \frac{2r^2(\rho_l - \rho_g)g}{9\mu_l}$$

When the spacing  $h$  is determined, it can be rearranged to calculate the bubble's escape time  $\tau$ :

$$\tau = \frac{h}{v_b}$$

### Computational details

The oxygen diffusion CFD simulation was conducted by ANSYS Fluent 2024R2. The Eulerian model was selected to calculate multiphase flow with the Primary Phase of potassium carbonate solution and the secondary phase of oxygen. The diameter of oxygen was set as 0.2 mm in the base case. The viscous model was set as Realizable k-epsilon Model. In the anode zone, the source terms of mass was set to describe the oxygen generation and the values were set according to the current

density at gaps of 1, 3, and 6 mm, respectively. The boundary conditions of oxygen outlets in the top and the bottom were set as Degasing, which was monitored for the oxygen separation rate. All other boundaries were set as wall. The operational conditions considered the gravity, which was  $-9.81 \text{ m}\cdot\text{s}^{-2}$  in the vertical direction. The solution method used the phase-coupled SIMPLE scheme for the pressure-velocity coupling. The PRESTO! scheme was selected for the pressure solution. Spatial discretization of the momentum, volume fraction, turbulent kinetic energy, and turbulent dissipation rate adopted the first-order upwind method. The initialization method used standard initialization. The convergence criteria were set to  $1e^{-4}$  for all residuals.

O<sub>2</sub> concentration uniformity index (UI) calculation formula:

$$UI = 1 - \frac{\frac{1}{A} \iint_A |\varphi(x) - \varphi_{avg}| dA}{2\varphi_{avg}}$$

where  $A$  is the area of a particular plane section.  $\varphi(x)$  is the local oxygen concentration at a point in the region.  $\varphi_{avg}$  is the average over that section or volume.

$$\varphi_{avg} = \frac{1}{A} \sum_{i=1}^n \varphi_i \Delta A_i$$

### Data availability

The main data that support the plots in this paper and other findings of this study are available within the article and its Supplementary Information. Source data are provided with this paper.

### References

1. Alkhadra, M. A. et al. Electrochemical methods for water purification, ion separations, and energy conversion. *Chem. Rev.* **122**, 13547–13635 (2022).
2. Botte, G. G. Electrochemical manufacturing in the chemical industry. *Interface Mag.* **23**, 49–55 (2014).
3. Chen, C., Khosrowabadi Kotyk, J. F. & Sheehan, S. W. Progress toward commercial application of electrochemical carbon dioxide reduction. *Chem* **4**, 2571–2586 (2018).
4. Wang, Y., Xue, Y. & Zhang, C. Electrochemical product engineering towards sustainable recovery and manufacturing of critical metals. *Green. Chem.* **23**, 6301–6321 (2021).
5. Mustain, W. E., Chatenet, M., Page, M. & Kim, Y. S. Durability challenges of anion exchange membrane fuel cells. *Energy Environ. Sci.* **13**, 2805–2838 (2020).
6. Varcoe, J. R. et al. Anion-exchange membranes in electrochemical energy systems. *Energy Environ. Sci.* **7**, 3135–3191 (2014).
7. Habibzadeh, F. et al. Ion exchange membranes in electrochemical CO<sub>2</sub> reduction processes. *Electrochem. Energy Rev.* **6**, 26 (2023).
8. Na, J. et al. General techno-economic analysis for electrochemical coproduction coupling carbon dioxide reduction with organic oxidation. *Nat. Commun.* **10**, 5193 (2019).
9. Sajna, M. S. et al. Electrochemical system design for CO<sub>2</sub> conversion: a comprehensive review. *J. Environ. Chem. Eng.* **11**, 110467–110467 (2023).
10. Belay, Z. A., Caleb, O. J. & Opara, U. L. Influence of initial gas modification on physicochemical quality attributes and molecular changes in fresh and fresh-cut fruit during modified atmosphere packaging. *Food Packag. Shelf Life* **21**, 100359 (2019).
11. Tsantil, E., Karaiskos, G. & Pontikis, C. Storage of fresh figs in low oxygen atmosphere. *J. Hortic. Sci. Biotechnol.* **78**, 56–60 (2003).
12. Baker, R. W. Future directions of membrane gas separation technology. *Ind. Eng. Chem. Res.* **41**, 1393–1411 (2002).

13. Chin, C., Kamin, Z., Bahrun, M. H. V. & Bono, A. The production of industrial-grade oxygen from air by pressure swing adsorption. *Int. J. Chem. Eng.* **2023**, e2308227 (2023).
  14. Shirley, A. I. & Lemcoff, N. O. High-purity nitrogen by pressure-swing adsorption. *AIChE J.* **43**, 419–424 (1997).
  15. Dhanushkodi, S. R., Capitanio, F., Biggs, T. & Mérida, W. Understanding flexural, mechanical and physico-chemical properties of gas diffusion layers for polymer membrane fuel cell and electrolyzer systems. *Int. J. Hydrog. Energy* **40**, 16846–16859 (2015).
  16. Rabiee, H. et al. Gas diffusion electrodes (GDEs) for electrochemical reduction of carbon dioxide, carbon monoxide, and dinitrogen to value-added products: a review. *Energy Environ. Sci.* **14**, 1959–2008 (2021).
  17. Rabiee, H. et al. Advances and challenges of carbon-free gas-diffusion electrodes (GDEs) for electrochemical CO<sub>2</sub> reduction. *Adv. Funct. Mater.* **35**, 28 (2024).
  18. Lauterborn, W. & Kurz, T. Physics of bubble oscillations. *Rep. Prog. Phys.* **73**, 106501 (2010).
  19. Stokes, G. G. *On the Effect of the Internal Friction of Fluids on the Motion of Pendulums*. (Pitt Press, 1844).
  20. Carr, D. & Kimble, M. C. Electrochemical oxygen separation from aircraft fuel tank ullage. *Meet. Abstr. Electrochem. Soc.* **MA2014-02**, 962–962 (2014).
  21. Fujita, Y., Nakamura, H. & Muto, T. An electrochemical oxygen separator using an ion-exchange membrane as the electrolyte. *J. Appl. Electrochem.* **16**, 935–940 (1986).
  22. Tseung, A. C. C. & Jasem, S. M. An integrated electrochemical-chemical method for the extraction of O<sub>2</sub> from air. *J. Appl. Electrochem.* **11**, 209–215 (1981).
  23. John Felix Kumar, R., Radhakrishnan, V. & Haridoss, P. Enhanced mechanical and electrochemical durability of multistage PTFE treated gas diffusion layers for proton exchange membrane fuel cells. *Int. J. Hydrog. Energy* **37**, 10830–10835 (2012).
  24. Reshetenko, T. V. et al. Multianalytical study of the PTFE content local variation of the PEMFC gas diffusion layer. *J. Electrochem. Soc.* **160**, F1305–F1315 (2013).
  25. Velayutham, G. Effect of micro-layer PTFE on the performance of PEM fuel cell electrodes. *Int. J. Hydrog. Energy* **36**, 14845–14850 (2011).
  26. Jessl, S. et al. Carbon nanotube conductive additives for improved electrical and mechanical properties of flexible battery electrodes. *Mater. Sci. Eng.: A* **735**, 269–274 (2018).
  27. Xu, H., Tong, X., Zhang, Y., Li, Q. & Lu, W. Mechanical and electrical properties of laminated composites containing continuous carbon nanotube film interleaves. *Compos. Sci. Technol.* **127**, 113–118 (2016).
  28. Erce Şengül Effect of gas diffusion layer characteristics and addition of pore-forming agents on the performance of polymer electrolyte membrane fuel cells. *Chem. Eng. Commun.* **196**, 161–170 (2008).
  29. Waseem, S. et al. Configuring the porosity and microstructure of carbon paper electrode using pore formers and its influence on the performance of PEMFC. *Energy Fuels* **34**, 16736–16745 (2020).
  30. Bar-On, I., Kirchain, R. & Roth, R. Technical cost analysis for PEM fuel cells. *J. Power Sourc.* **109**, 71–75 (2002).
  31. Taleb, A., Maine, E. & Kjeang, E. Technical-economic cost modeling as a technology management tool. *J. Manuf. Technol. Manag.* **25**, 279–298 (2014).
- Natural Science Foundation of China (U23A2081 Y.W.), the Anhui Provincial Natural Science Foundation (2208085UD04, 2108085UD06 Y.W.), the Key Technologies R & D Program of Anhui Province (2023z04020010 and 2022a05020053 Y.W.), the Joint Funds from Hefei National Synchrotron Radiation Laboratory (KY2060000180 and KY206000019), the Fundamental Research Funds for the Centre Universities (WK9990000155 Y.Z.) and USTC Research Funds of the Double First-Class Initiative (YD2060006005 Y.W.). This work was partially carried out at the USTC Center for Micro and Nanoscale Research and Fabrication. We acknowledge the Experimental Center of Engineering and Material Science in the University of Science and Technology of China. We thank the photoemission end stations BL1W1B in Beijing Synchrotron Radiation Facility (BSRF), BL14W1 in Shanghai Synchrotron Radiation Facility (SSRF), BL10B and BL11U in National Synchrotron Radiation Laboratory (NSRL) for the help in characterizations.

## Author contributions

G.L., Y.Z., and Y.W. conceived the idea and designed the experiments. P.L., X.Z., W.S., Y.T., D.L., C.Z., F.Z., Z.W., J.T., and Y.Z. performed most experiments, including the sample synthesis, characterization, and measurements. P.J. performed the XAFS data fitting. X.T. performed the oxygen diffusion CFD simulation. G.L. provided suggestions and guidance about the theoretical analysis. P.L., J.T., G.L., Y.Z., and Y.W. co-wrote the paper. Y.Z. and Y.W. supervised P.L. All authors reviewed and commented on the manuscript.

## Competing interests

The authors declare no competing interests.

## Additional information

**Supplementary information** The online version contains supplementary material available at <https://doi.org/10.1038/s41467-025-59506-7>.

**Correspondence** and requests for materials should be addressed to Jun Tang, Guiqiang Li, Yu Zhang or Yuen Wu.

**Peer review information** *Nature Communications* thanks the anonymous, reviewer(s) for their contribution to the peer review of this work. A peer review file is available.

**Reprints and permissions information** is available at <http://www.nature.com/reprints>

**Publisher's note** Springer Nature remains neutral with regard to jurisdictional claims in published maps and institutional affiliations.

**Open Access** This article is licensed under a Creative Commons Attribution-NonCommercial-NoDerivatives 4.0 International License, which permits any non-commercial use, sharing, distribution and reproduction in any medium or format, as long as you give appropriate credit to the original author(s) and the source, provide a link to the Creative Commons licence, and indicate if you modified the licensed material. You do not have permission under this licence to share adapted material derived from this article or parts of it. The images or other third party material in this article are included in the article's Creative Commons licence, unless indicated otherwise in a credit line to the material. If material is not included in the article's Creative Commons licence and your intended use is not permitted by statutory regulation or exceeds the permitted use, you will need to obtain permission directly from the copyright holder. To view a copy of this licence, visit <http://creativecommons.org/licenses/by-nc-nd/4.0/>.

© The Author(s) 2025

## Acknowledgements

This work was supported by National Key R&D Program of China (2021YFA1501003 M.Z.), the National Natural Science Foundation of China (92261105 and 22221003 Y.W.), the Joint Funds of the National